SCIENCE CHINA Materials ARTICLES

mater.scichina.com link.springer.com

Published online 14 November 2019 | https://doi.org/10.1007/s40843-019-1214-y

Sci China Mater 2020, 63(3): 413–420

Layer dependence of stacking order in nonencapsulated few-layer CrI_3

Kai Guo[1,4], Bowen Deng[3], Zhen Liu[1,4], Chaofeng Gao[2], Zhongtai Shi[1,4], Lei Bi[1,4], Li Zhang[1,4], Haipeng Lu[1,4], Peiheng Zhou[1,4], Linbo Zhang[1,4*], Yingchun Cheng[2] and Bo Peng[1,4*]

ABSTRACT Long-range magnetic orders in atomically thin ferromagnetic CrI_3 trigger new fascinating physics and application perspectives. The physical properties of two-dimensional (2D) ferromagnetism CrI_3 are significantly influenced by interlayer spacing and stacking order, which are sensitive to the hydrostatic pressure and external environments. However, there remains debate on the stacking order at low temperature. Here, we study the interlayer coupling and stacking order of non-encapsulated 2–5 layer and bulk CrI_3 at 10 K by Raman spectroscopy; demonstrate a rhombohedral stacking in both antiferromagnetic and ferromagnetic CrI_3. The opposite helicity dependence of A_g and E_g modes arising from phonon symmetry further validates the rhombohedral stacking. An anomalous temperature-dependent behavior is observed due to spin-phonon coupling below 60 K. Our study provides insights into the interlayer coupling and stacking orders of 2D ferromagnetic materials.

Keywords: ferromagnetic 2D materials, Ising ferromagnet, spintronics, magneto-optical

INTRODUCTION

Since the discovery of two ferromagnetic atomically thin CrI_3 and $Cr_2Ge_2Te_6$ in 2017, intrinsic ferromagnetism in two-dimensional (2D) van der Waals (vdW) materials, maintaining long-range magnetic orders at the atomic monolayer limit, has received increasing attention [1–7]. 2D vdW ferromagnetic materials as spin-filters have been integrated into vdW heterostructures, demonstrating giant tunneling magnetoresistance towards the next-generation information transfer and data storage technologies [8–10]. Among 2D ferromagnetic materials, CrI_3 is of particular interest. Bulk CrI_3 is ferromagnetic below the Curie temperature (T_C), but few-layer CrI_3 displays striking layer-dependent magnetism. Each individual layer is ferromagnetic; however, adjacent layers are antiferromagnetically coupled together and could become a layered antiferromagnet when thinned down to a few atomic layers [1]. The interlayer magnetic state can be switched between ferromagnetic and antiferromagnetic by electric gating or electrostatic doping [11–14] and pressure [15,16].

In a vdW material and heterostructures, a tiny change of lattice constant and interlayer coupling between adjacent layers can drastically influence their physical properties. Bulk CrI_3 adopts the monoclinic stacking at room temperature, while transfers to rhombohedral stacking at ~210 K. Bulk and encapsulated few-layer CrI_3 with rhombohedral stacking have been reported to be ferromagnetic below ~61 K [17,18]. However, recent experiments demonstrate that the BN-encapsulated bi- and few-layer CrI_3 and $CrCl_3$ belong to monoclinic structure (point group C_{2h} (2/*m*)) rather than rhombohedral structure at low temperature [19,20], and some theoretical proposals demonstrate that the antiferromagnetic coupling is associated with monoclinic layer stacking [21]. Thus, there is still a debate on the stacking order of CrI_3 at low temperature.

[1] National Engineering Research Center of Electromagnetic Radiation Control Materials, School of Electronic Science and Engineering, University of Electronic Science and Technology of China, Chengdu 611731, China
[2] Key Laboratory of Flexible Electronics & Institute of Advanced Materials, Jiangsu National Synergetic Innovation Center for Advanced Materials, Nanjing Tech University, Nanjing 211816, China
[3] Department of Physics, Broida Hall, University of California Santa Barbara, CA 93106-9530, USA
[4] Key Laboratory of Multi-spectral Absorbing Materials and Structures of Ministry of Education, University of Electronic Science and Technology of China, Chengdu 611731, China
* Corresponding authors (emails: bo_peng@uestc.edu.cn (Peng B); zhanglinbo@uestc.edu.cn (Zhang L))

A complete understanding of the low-temperature lattice structure and stacking order is crucial for 2D vdW ferromagnetic materials. Raman spectroscopy is a powerful tool to study the crystal structures, lattice vibration and shift and interlayer coupling [22–28]. In this study, we investigate the layer, polarization and helicity dependencies of Raman features of non-encapsulated 2–5 layer and bulk CrI_3 at 10 K, demonstrating that few-layer and bulk CrI_3 are rhombohedral phase at low temperature, including antiferromagnetic bilayer CrI_3. The peak intensities of E_g^3 and E_g^4 mode are independent of the polarization angle, while the intensities of A_g^2 and A_g^3 show a two-fold polarization dependence. The polarization-resolved Raman spectra demonstrate that the A_g^3 and E_g^4 features show opposite helicities in which the A_g^3 mode maintains the helicity of incident light; however, the E_g^4 mode reverses it. Under cooling, the A_g^3 and E_g^4 modes shift to higher frequencies; remarkably, a spin-phonon coupling takes place and causes an anomalous behavior for the Raman feature below ~60 K.

EXPERIMENTAL METHODS

Sample preparation

Few-layer CrI_3 was mechanically exfoliated from a bulk crystal onto polydimethylsiloxane films and was then directly transferred onto SiO_2/Si substrates, which was then loaded into the cold head for optical measurements in a glove box filled with Ar.

Optical measurements

The Raman signals were recorded using a Witec Alpha 300R Plus confocal Raman microscope with a closed cycle optical cryostat (10 K) and a 7 T magnetic field. A power-stabilized 633 nm HeNe laser was modulated by photoelastic modulator (PEM) and coupled to the Witec Raman system. The modulated beam was directed through a non-polarizing beamsplitter cubes to the sample, housed in a closed-cycle cryostat at 10 K. An out-of-plane magnetic field was applied in Faraday geometry. The reflected beam passed through the same non-polarizing beamsplitter cubes, non-PM multimode fiber onto a photodetector, where lock-in detection measured the reflected intensity at f_{PEM} (50 kHz). A long working distance 50× objective (NA = 0.45) was used for the Raman and reflective magnetic circular dichroism (RMCD) measurements. The Raman signals were coupled into the spectrometer with an 1800 and 600 g mm^{-1} grating. $1/4\lambda$ waveplate and polarization analyzer were used for the polarization-resolved Raman measurements. The power of a 514 nm laser was measured to be approximately 2 mW, and the typical integration time was 30 s.

RESULTS AND DISCUSSION

Layer dependence of magnetic order

In 2D ferromagnetic CrI_3, the Cr^{3+} ions in each layer are coordinated by six nonmagnetic I^- ions to form an octahedral geometry, which further share edges to build a honeycomb network (Fig. 1a). Bulk CrI_3 crystals undergo a phase transition to a rhombohedral structure (space group $R\bar{3}$, Fig. 1b) at ~210–220 K from a monoclinic structure (space group $C2/m$, Fig. 1c) at room temperature [17]. Fig. 1d shows the non-encapsulated CrI_3 with 2–6 layers on SiO_2 (300 nm)/Si substrates, which are *in-situ* loaded into cold head with an optical window in the glovebox. The different numbers of layers can be identified through the optical contrast. Our experimental optical contrast results shown in Fig. 1e (red circles) are consistent with the reported experimental and calculated results from Xu *et al.* [1] (solid blue line in Fig. 1e). Bulk CrI_3 crystals show distinct ferromagnetism below ~65 K (Fig. 1f).

Fig. 2 shows the RMCD signal in atomically-thin CrI_3 at 10 K. RMCD signals from a bilayer CrI_3 flake approach zero when applied magnetic fields ± 0.65 T, indicating antiferromagnetic behavior (Fig. 2a). In bilayer CrI_3, the two layers have opposite magnetic orientation and nearly compensate for the intrinsic magnetocrystalline anisotropy each other; therefore, the net magnetization disappear and 2-layer (2L) CrI_3 is antiferromagnetic [1,2]. However, striking hysteresis is observed in 3L and 4L CrI_3 flakes (Fig. 2b, c). In 3L CrI_3, the magnetizations of the three layers are oriented to the same direction, while the magnetization of one layer is opposite with the other three in 4L CrI_3. Thus, the net magnetization of 3L CrI_3 is stronger than that of 4L CrI_3.

Layer dependence of stacking order

The stacking order and crystal structures of non-encapsulated few-layer CrI_3 can be identified by polarized Raman spectroscopy. The polarization selection rules were performed on a 2–5 layer (2L, 3L, 4L and 5L) and bulk CrI_3 at 10 K using a confocal Raman microscope system with a backscattering geometry (Fig. 3a–d). The incident and scattered light are along the $-Z$ and $+Z$ direction, respectively. The polarization configuration of

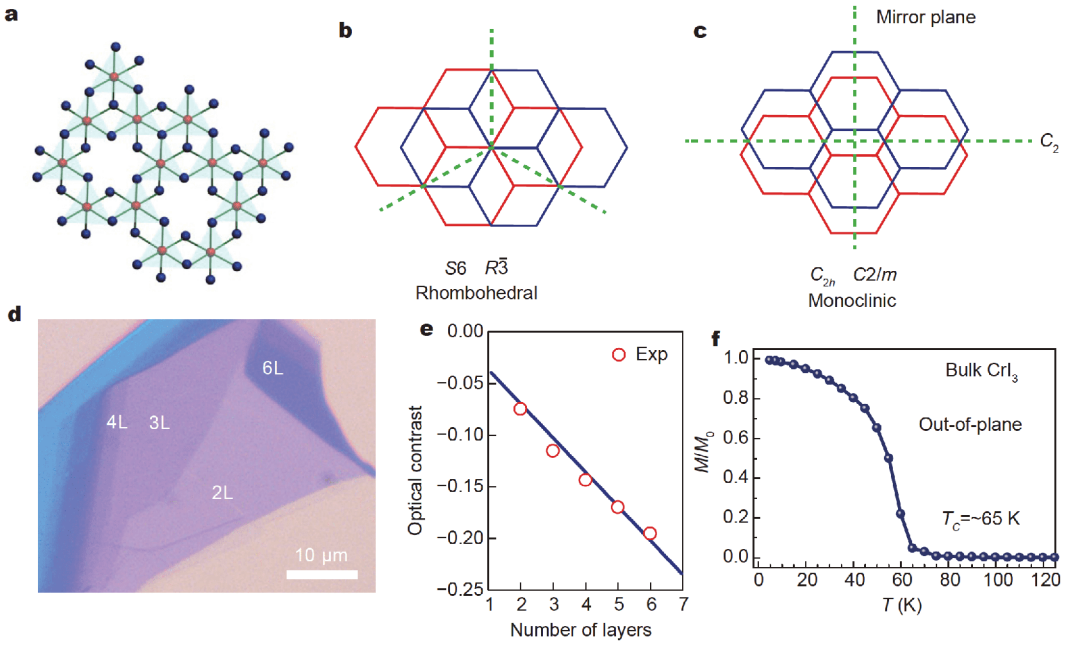

Figure 1 Exfoliated few-layer CrI_3. (a) Atomic structures of monolayer CrI_3. (b, c) Rhombohedral (b) and monoclinic (c) stacking order in bilayer CrI_3. The rhombohedral structure has an out-of-plane C_3 axis and a symmetric center ($S_6 = C_3 + i$), while the monoclinic structure has an in-plane C_2 axis and a mirror plane. (d) Optical micrograph of the exfoliated few-layer CrI_3. (e) Optical contrast of the CrI_3 samples with different numbers of layers (red circles). The blue solid line is the calculated results based on Fresnel's equations [1]. (f) Magnetization of bulk CrI_3 as a function of temperature, indicating T_C = ~65 K.

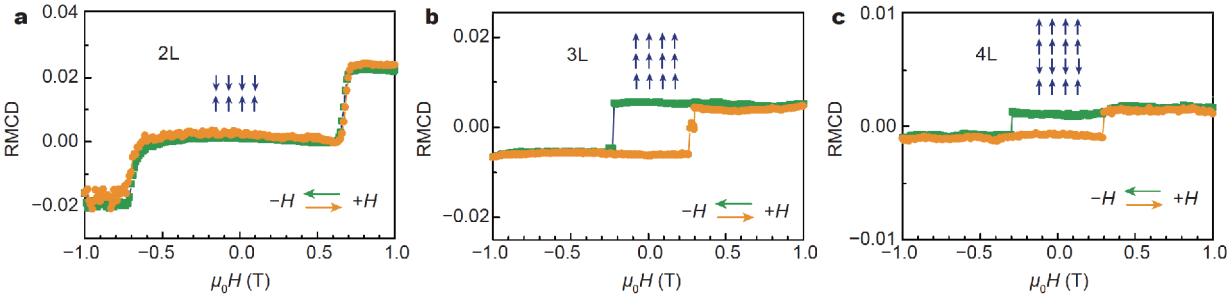

Figure 2 Layer-dependent magnetic ordering in atomically-thin CrI_3 at 10 K. RMCD signal on a 2L (a), 3L (b) and 4L (c) CrI_3 flake, showing antiferromagnetic behavior in bilayer CrI_3 and ferromagnetic behavior in 3L and 4L CrI_3. The blue arrows indicate the magnetization orientation in different layers.

the incident and scattered light are parallel (*XX*) or perpendicular (*XY*) to each other. The feature at ~103 and 128 cm^{-1} is only present in the parallel configuration (*XX*), while the Raman peaks at ~107 and ~238 cm^{-1} appear for both parallel and perpendicular configurations (*XX* and *XY*). The Raman scattering intensities *I* are proportional to $|\boldsymbol{e}_s \cdot \boldsymbol{R} \cdot \boldsymbol{e}_i|^2$, where $\boldsymbol{e}_i$ and $\boldsymbol{e}_s$ are the polarization unit vectors of the incident and scattered light, respectively [26,29,30]. $\boldsymbol{R}$ is the Raman tensor of the Raman-active vibrational modes as predicted by group theory.

We consider both the rhombohedral (point group, C_{3i}) and monoclinic phase (point group, C_{2h}). The scattered light polarization has an angle of θ with that of the incident light, which is parallel to the *x*-axis. Thus, $\hat{\boldsymbol{e}}_i = (1, 0, 0)$ and $\hat{\boldsymbol{e}}_s = (\cos\theta, \sin\theta, 0)$, and $\theta = 0^o$ and 90^o under the *XX* and *XY* polarization configuration.

In rhombohedral structure, Raman active modes are the A_g and E_g modes and the corresponding Raman tensors are given by [31]

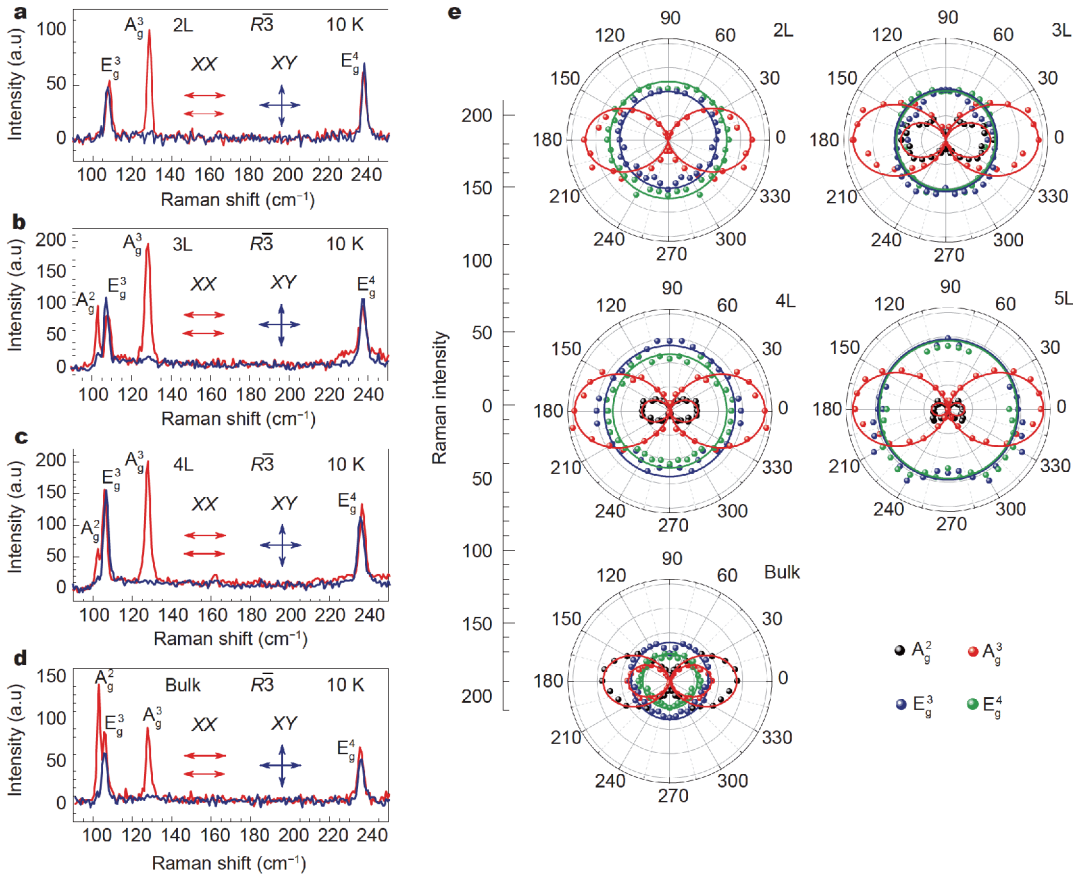

Figure 3 Layer dependence of the stacking orders in CrI_3 at 10 K. Raman spectra of 2L (a), 3L (b), 4L (c) and bulk CrI_3 (d) in the parallel (*XX*, red curve) and perpendicular (*XY*, blue curve) polarization selection channels. (e) Polarization angle dependence of Raman intensity in 2–5 layer and bulk CrI_3. The Raman features at ~107 and ~234 cm^{-1} are degenerated E_g^3 and E_g^4 mode for the Rhombohedral phase, whose intensities are independent of the polarization angle; in contrast, the A_g^2 and A_g^3 modes at ~103 and 128 cm^{-1} show distinct a two-fold polarization dependence.

$$\mathrm{A_g}(\boldsymbol{R}):\begin{pmatrix} a & 0 & 0\\ 0 & a & 0\\ 0 & 0 & b\end{pmatrix},\ {}^1\mathrm{E_g}(\boldsymbol{R}):\begin{pmatrix} c & d & e\\ d & -c & f\\ e & f & 0\end{pmatrix},$$
$$(1)$$
$${}^2\mathrm{E_g}(\boldsymbol{R}):\begin{pmatrix} d & -c & -f\\ -c & -d & e\\ -f & e & 0\end{pmatrix}.$$

Taking $\boldsymbol{e}_i$, $\boldsymbol{e}_s$ and $\boldsymbol{R}$ to $I\propto\left|\boldsymbol{e}_s\cdot\boldsymbol{R}\cdot\boldsymbol{e}_i\right|^2$, the Raman intensities of A_g and E_g are

$$I_{\mathrm{A_g}}(\boldsymbol{R})\propto a^2\cos^2\theta,$$
$${}^1I_{\mathrm{E_g}}(\boldsymbol{R})\propto c^2\cos^2\theta+cd\sin(2\theta)+d^2\sin^2\theta,$$
$${}^2I_{\mathrm{E_g}}(\boldsymbol{R})\propto d^2\cos^2\theta-cd\sin(2\theta)+c^2\sin^2\theta. \quad (2)$$

The E_g modes are degenerated. All E_g modes contribute to a peak at the same frequency, so the Raman intensities of E_g modes can be expressed as

$$I_{\mathrm{E_g}}(\boldsymbol{R})={}^1I_{\mathrm{E_g}}(\boldsymbol{R})+{}^2I_{\mathrm{E_g}}(\boldsymbol{R})=c^2+d^2, \quad (3)$$

as a constant, and the E_g modes are independent of the polarization, which can be detected in any polarization configuration. In contrast, the A_g modes show striking two-fold polarization dependence, which can be observed only in parallel polarization configuration.

In monoclinic structure, the symmetry is lowered and the E_g modes split to an A_g and a B_g mode. Thus, only the A_g and B_g modes are active and corresponding Raman tensors are given by

$$\mathrm{A_g}(\boldsymbol{M}):\begin{pmatrix} a & 0 & d\\ 0 & b & 0\\ d & 0 & c\end{pmatrix},\ \mathrm{B_g}(\boldsymbol{M}):\begin{pmatrix} 0 & e & 0\\ e & 0 & f\\ 0 & f & 0\end{pmatrix}. \quad (4)$$

The Raman intensities of A_g and B_g can be expressed as

$$I_{A_g}(\boldsymbol{M}) \propto a^2\cos^2\theta,\ I_{B_g}(\boldsymbol{M}) \propto e^2\sin^2\theta. \quad (5)$$

Thus, the Raman intensities of A_g and B_g modes have opposite two-fold dependence on polarization angle in the monoclinic phase.

Therefore, group theory predicts that the Raman scattering intensity is zero for A_g modes under the perpendicular (*XY*) configuration in both the rhombohedral and monoclinic stacking [30]. However, only for rhombohedral phase, there remain the polarization-independent E_g modes that have nonzero Raman intensities under the parallel (*XX*) and perpendicular (*XY*) configurations. The polarization angle dependences of the features at ~103, ~107, ~128 and ~234 cm^{-1} of non-encapsulated 2–5 layer and bulk CrI_3 are shown in Fig. 3e. The Raman intensities of the peaks near 103 and 128 cm^{-1} have a two-fold pattern *versus* polarization angle; in contrast, the modes at ~107 and ~234 cm^{-1} are independent of the polarization angle. Therefore, the non-encapsulated 2–5 layer and bulk CrI_3 are rhombohedral phase rather than monoclinic phase; and the peaks at ~103, ~107, ~128 and ~234 cm^{-1} are assigned to the A_g^2, E_g^3, A_g^3 and E_g^4 modes, respectively [18].

To further validate the rhombohedral stacking of CrI_3 at low temperature, the helicity selection rules were studied at 10 K (Fig. 4). Fig. 4a shows a schematic of the experimental optical setup. The linearly polarized light passes through a 1/4λ waveplate and transfers to circularly polarized incident $e_i = E_0 e^{i(kz-wt)}(\hat{x} \pm i\hat{y})$. The incident and scattered light are along opposite direction, and thus, the scattered light e_s is $E_0 e^{i(kz-wt)}(\hat{x} \mp i\hat{y})$ and $E_0 e^{i(kz-wt)}(\hat{x} \pm i\hat{y})$ under the same (σ+σ+) and opposite (σ+σ−) circular polarization configuration, respectively.

The Raman intensities of the A_g modes in rhombohedral phase can be expressed as

$$I_{A_g}^{\sigma+\sigma+}(\boldsymbol{R}) \propto a^2,\ I_{A_g}^{\sigma+\sigma-}(\boldsymbol{R}) \propto 0. \quad (6)$$

On the contrary, the Raman intensities of the E_g modes can be expressed as

$$I_{E_g}^{\sigma+\sigma+}(\boldsymbol{R}) \propto 0,\ I_{E_g}^{\sigma+\sigma-}(\boldsymbol{R}) \propto c^2 + d^2. \quad (7)$$

As shown in Equations (6, 7), the A_g modes maintain the helicity of incident light; however, the E_g modes re-

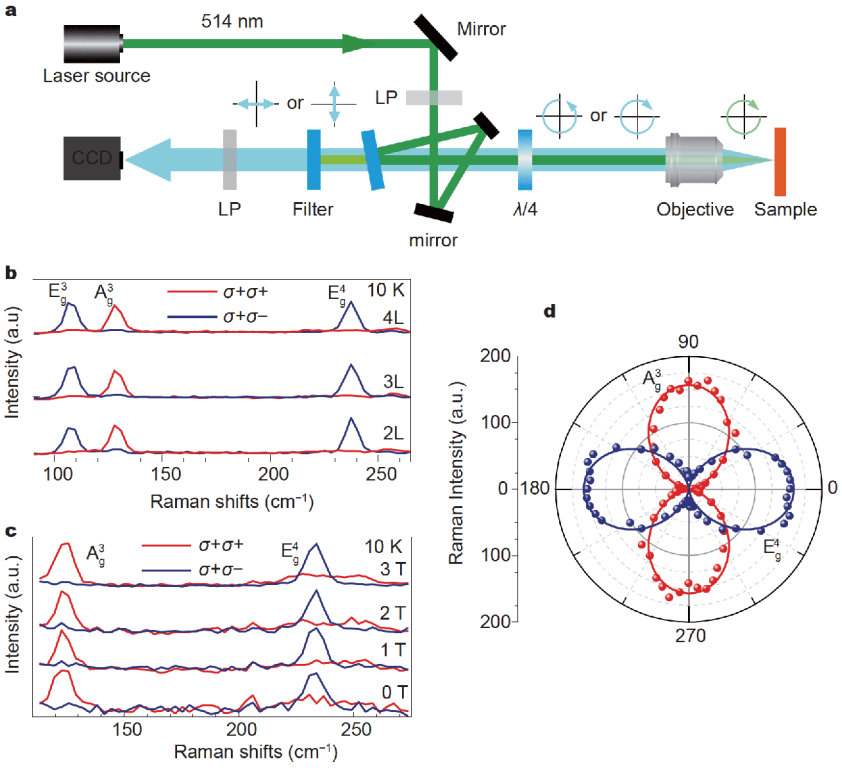

Figure 4 Helicity-resolved Raman spectra at 10 K. (a) Schematic of the helicity-resolved experimental optical setup. (b) Helicity-resolved Raman spectra of 2L, 3L and 4L CrI_3. (c) Helicity-resolved Raman spectra of 3L CrI_3 as a function of the magnetic field. (d) Corresponding angular dependence of the A_g^3 and E_g^4 mode intensities for 3L CrI_3, showing a distinctly opposite helicity.

verse it. In contrast, for monoclinic phase with lower symmetry, both the A_g and B_g modes reverse the helicity of incident light, in which the Raman intensities of A_g and B_g modes are given by

$$I_{A_g}^{\sigma+\sigma+}(\boldsymbol{M}) \propto 0,\ I_{A_g}^{\sigma+\sigma-}(\boldsymbol{M}) \propto a^2,$$
$$I_{B_g}^{\sigma+\sigma+}(\boldsymbol{M}) \propto 0,\ I_{B_g}^{\sigma+\sigma-}(\boldsymbol{M}) \propto e^2. \quad (8)$$

The polarization-resolved Raman spectra were obtained under excitation by a left-handed circularly polarized light at 2.41 eV (σ+). Remarkably, the Raman features of 2L, 3L and 4L CrI_3 at ~128 cm^{-1} have the same helicity as the incident photon, whereas the peaks at ~234 cm^{-1} switch the helicity (Fig. 4b and c). The striking opposite polarization dependence of helicities of the two Raman modes is shown in Fig. 4d. The experimental data are in agreement with the predicted rhombohedral phase results. The helicity-dependent experimental results further validate that the peaks at ~128 and ~234 cm^{-1} are assigned to the A_g^3 and E_g^4 modes, respectively, consistent with above polarization-resolved Raman results. With increasing magnetic field, the helicity selection behaviors show no detectable changes (Fig. 4c), indicating that this is independent of the external magnetic field. The helicity selection behaviors are only attributed to the symmetric Raman tensors. Thus, 2–5 layer and bulk 2D ferromagnetic CrI_3 have rhombohedral stacking order.

Temperature dependence of the Raman features

To better understand the lattice dynamics, the temperature dependence of the Raman features was determined in 2L, 3L and 6L CrI_3 flakes. Since the transition from the monoclinic phase to the rhombohedral phase occurs at around 210–220 K in CrI_3 [17], we focus on investigating the Raman features below 200 K. Fig. 5a–c show the normalized Raman intensity maps of the 2L, 3L and 6L CrI_3 with decreasing temperatures from 200 to 10 K. The A_g^3 and E_g^4 modes simultaneously blueshift to higher frequencies with decreasing temperatures, which are attributed to the phonon anharmonic decay and lattice contraction. The shifts of the A_g^3 modes are ~1.4, ~0.9 and ~0.8 cm^{-1} for the 2L, 3L and 6L CrI_3, and the E_g^4 modes show shifts of ~2.9, ~2.9 and ~2.4 cm^{-1}, respectively.

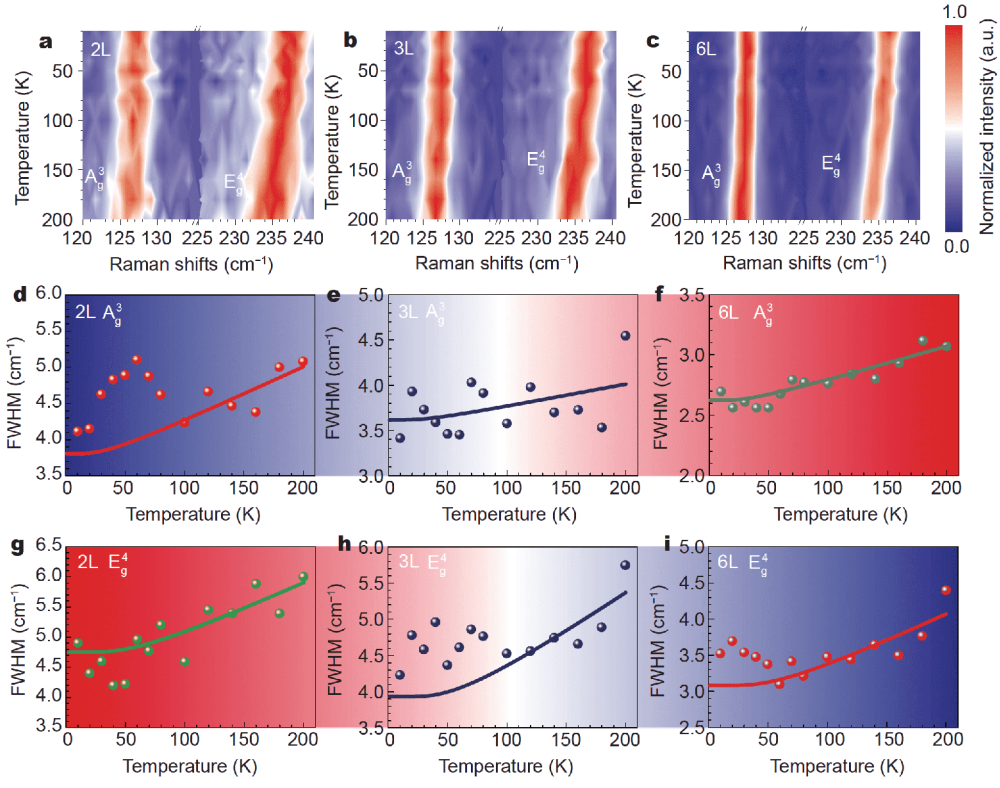

Figure 5 Temperature dependence of the A_g^3 and E_g^4 Raman modes. (a–c) Normalized Raman intensity maps of the 2L, 3L and 6L CrI_3 as a function of temperature. The Raman features shift to higher frequencies with decreasing temperatures. (d–i) The linewidths of the A_g^3 and E_g^4 Raman features as a function of temperature as extracted from Fig. 3a, b. The sudden increases in the linewidths indicate the occurrence of spin-phonon coupling.

The linewidths for the A_g^3 and E_g^4 modes are extracted to investigate the spin-phonon coupling behavior. Fig. 5d–i show the linewidths of the A_g^3 and E_g^4 modes of 2L, 3L and 6L CrI_3 with decreasing temperature from 200 to 10 K. The temperature dependence of the linewidths is predicted by phonon-phonon coupling [32], which is given by

$$\Gamma_L(T) = \Gamma_{L,0}(1 + 2\lambda_{\text{ph-ph}} / (\exp(hC\omega_0 / 2k_BT) - 1)), \quad (9)$$

where the $\Gamma_{L,0}$ and ω_0 are the zero temperature limits of the linewidth and phonon energy, obtained by extrapolating the experimental results to 0 K. The $\lambda_{\text{ph-ph}}$ represents the phonon-phonon coupling constant. Above 60 K ($\sim T_C$), the linewidths of the A_g^3 and E_g^4 modes monotonically decrease as the temperature decreases (solid lines in Fig. 5d–i). However, the linewidths deviate from the expected tendency below 60 K. In particular, the A_g^3 (E_g^4) modes of the 2L (6L) CrI_3 exhibit distinct deviation behavior (Fig. 5d–i), which indicates that a new scattering mechanism contributes to the anomalous phonon behavior. The T_C of few-layer CrI_3 is ~65 K (Fig. 1f) [3]. The emerging long-range magnetic order is anticipated to result in the abrupt change in the linewidth originating from spin-phonon coupling. We briefly discuss the mechanism of spin-phonon coupling. The total Hamiltonian of lattice in crystals is expressed as

$$H = H_{\text{ion}} + H_{\text{electron}} + H_{\text{e-ph}}. \quad (10)$$

In the presence of magnetic orders, an additional Hamiltonian term is given by

$$H_{\text{spin}} = -\sum_{i,j} J_{ij} \langle S_i S_j \rangle, \quad (11)$$

where J_{ij} is the spin-phonon coupling constant and $\langle S_i S_j \rangle$ is spin correlation function [33]. In 2D layered CrI_3 materials, the electron-phonon coupling was not observed, thus the Hamiltonian $H_{\text{e-ph}}$ was neglected and only phonon-phonon coupling was considered. Thus, the total potential energy of a Raman active mode consists of "lattice" and "spin" contributions; corresponding Hamiltonian of Raman modes is expressed as

$$H = H_{\text{ion}} + H_{\text{electron}} + H_{\text{spin}} = H_{\text{lattice}} + H_{\text{spin}}. \quad (12)$$

Therefore, the spin-phonon exchange interaction takes place in the ferromagnetic phase at low temperature, resulting in the deviation of linewidth.

CONCLUSION

In summary, we demonstrated a comprehensive understanding of stacking order of 2D ferromagnetic CrI_3, including layer, polarization and temperature dependence of A_g and E_g modes. The non-encapsulated 2–5 layer and bulk CrI_3 are rhombohedral stacking order at 10 K, rather than monoclinic structure. The spin-phonon coupling occurs below ~60 K, resulting in the deviation of linewidth. Zero-momentum spin wave features close to the A_g mode in frequency have been observed [34]. This work highlights the potential to manipulate spin waves through spin-phonon and magnetoelectric coupling in new ferromagnetic 2D materials to produce novel spintronic devices [35].

Received 31 October 2019; accepted 1 November 2019; published online 14 November 2019

1 Huang B, Clark G, Navarro-Moratalla E, *et al.* Layer-dependent ferromagnetism in a van der Waals crystal down to the monolayer limit. Nature, 2017, 546: 270–273
2 Gong C, Li L, Li Z, *et al.* Discovery of intrinsic ferromagnetism in two-dimensional van der Waals crystals. Nature, 2017, 546: 265–269
3 Zhong D, Seyler KL, Linpeng X, *et al.* van der Waals engineering of ferromagnetic semiconductor heterostructures for spin and valleytronics. Sci Adv, 2017, 3: e1603113
4 Deng Y, Yu Y, Song Y, *et al.* Gate-tunable room-temperature ferromagnetism in two-dimensional Fe_3GeTe_2. Nature, 2018, 563: 94–99
5 Mounet N, Gibertini M, Schwaller P, *et al.* Two-dimensional materials from high-throughput computational exfoliation of experimentally known compounds. Nat Nanotech, 2018, 13: 246–252
6 Lee JU, Lee S, Ryoo JH, *et al.* Ising-type magnetic ordering in atomically thin $FePS_3$. Nano Lett, 2016, 16: 7433–7438
7 Bonilla M, Kolekar S, Ma Y, *et al.* Strong room-temperature ferromagnetism in VSe_2 monolayers on van der Waals substrates. Nat Nanotech, 2018, 13: 289–293
8 Song T, Cai X, Tu MWY, *et al.* Giant tunneling magnetoresistance in spin-filter van der Waals heterostructures. Science, 2018, 360: 1214–1218
9 Klein DR, MacNeill D, Lado JL, *et al.* Probing magnetism in 2D van der Waals crystalline insulators *via* electron tunneling. Science, 2018, 360: 1218–1222
10 Wang Z, Gutiérrez-Lezama I, Ubrig N, *et al.* Very large tunneling magnetoresistance in layered magnetic semiconductor CrI_3. Nat Commun, 2018, 9: 2516
11 Huang B, Clark G, Klein DR, *et al.* Electrical control of 2D magnetism in bilayer CrI_3. Nat Nanotech, 2018, 13: 544–548
12 Jiang S, Shan J, Mak KF. Electric-field switching of two-dimensional van der Waals magnets. Nat Mater, 2018, 17: 406–410
13 Jiang S, Li L, Wang Z, *et al.* Controlling magnetism in 2D CrI_3 by electrostatic doping. Nat Nanotech, 2018, 13: 549–553
14 Wang Z, Zhang T, Ding M, *et al.* Electric-field control of magnetism in a few-layered van der Waals ferromagnetic semiconductor. Nat Nanotech, 2018, 13: 554–559
15 Li T, Jiang S, Sivadas N, *et al.* Pressure-controlled interlayer magnetism in atomically thin CrI_3. Nat Mater, 2019, 18: 1303–1308
16 Song T, Fei Z, Yankowitz M, *et al.* Switching 2D magnetic states

via pressure tuning of layer stacking. Nat Mater, 2019, 18: 1298–1302
17 McGuire MA, Dixit H, Cooper VR, *et al.* Coupling of crystal structure and magnetism in the layered, ferromagnetic insulator CrI_3. Chem Mater, 2015, 27: 612–620
18 Djurdjić-Mijin S, Šolajić A, Pešić J, *et al.* Lattice dynamics and phase transition in CrI_3 single crystals. Phys Rev B, 2018, 98: 104307
19 Sun Z, Yi Y, Song T, *et al.* Giant nonreciprocal second-harmonic generation from antiferromagnetic bilayer CrI_3. Nature, 2019, 572: 497–501
20 Klein DR, MacNeill D, Song Q, *et al.* Enhancement of interlayer exchange in an ultrathin two-dimensional magnet. Nat Phys, 2019, 15: 1255–1260
21 Sivadas N, Okamoto S, Xu X, *et al.* Stacking-dependent magnetism in bilayer CrI_3. Nano Lett, 2018, 18: 7658–7664
22 Webster L, Liang L, Yan JA. Distinct spin–lattice and spin–phonon interactions in monolayer magnetic CrI_3. Phys Chem Chem Phys, 2018, 20: 23546–23555
23 Sun L, Zheng J. Optical visualization of MoS_2 grain boundaries by gold deposition. Sci China Mater, 2018, 61: 1154–1158
24 Wu S, Shi X, Liu Y, *et al.* The influence of two-dimensional organic adlayer thickness on the ultralow frequency Raman spectra of transition metal dichalcogenide nanosheets. Sci China Mater, 2019, 62: 181–193
25 Zhao W, Ghorannevis Z, Amara KK, *et al.* Lattice dynamics in mono- and few-layer sheets of WS_2 and WSe_2. Nanoscale, 2013, 5: 9677–9683
26 Zhang X, Qiao XF, Shi W, *et al.* Phonon and raman scattering of two-dimensional transition metal dichalcogenides from monolayer, multilayer to bulk material. Chem Soc Rev, 2015, 44: 2757–2785
27 Xiao Y, Zhou M, Liu J, *et al.* Phase engineering of two-dimensional transition metal dichalcogenides. Sci China Mater, 2019, 62: 759–775
28 Ren J, Teng C, Cai Z, *et al.* Controlled one step thinning and doping of two-dimensional transition metal dichalcogenides. Sci China Mater, 2019, 62: 1837–1845
29 Lu X, Luo X, Zhang J, *et al.* Lattice vibrations and Raman scattering in two-dimensional layered materials beyond graphene. Nano Res, 2016, 9: 3559–3597
30 Zhao Y, Luo X, Li H, *et al.* Interlayer breathing and shear modes in few-trilayer MoS_2 and WSe_2. Nano Lett, 2013, 13: 1007–1015
31 Loudon R. The Raman effect in crystals. Adv Phys, 1964, 13: 423–482
32 Baum A, Milosavljević A, Lazarević N, *et al.* Phonon anomalies in FeS. Phys Rev B, 2018, 97: 054306
33 Granado E, García A, Sanjurjo JA, *et al.* Magnetic ordering effects in the Raman spectra of $La_{1-x}Mn_{1-x}O_3$. Phys Rev B, 1999, 60: 11879–11882
34 Jin W, Kim HH, Ye Z, *et al.* Raman fingerprint of two terahertz spin wave branches in a two-dimensional honeycomb Ising ferromagnet. Nat Commun, 2018, 9: 5122
35 Yao X, Ma J, Lin Y, *et al.* Magnetoelectric coupling across the interface of multiferroic nanocomposites. Sci China Mater, 2015, 58: 143–155

Acknowledgements We acknowledge the financial support from the National Natural Science Foundation of China (51602040 and 51872039), the Science and Technology Program of Sichuan (M112018JY0025) and the Scientific Research Foundation for New Teachers of UESTC (A03013023601007).

Author contributions Peng B developed the concept, designed the experiment and prepared the manuscript. Cheng Y synthesized the CrI_3 crystal. Deng B, Guo K, Liu Z, Gao C and Shi Z prepared the CrI_3 samples and performed the Raman measurements. Bi L, Zhou P, Zhang L, Lu H and Zhang L contributed to mechanism of Raman scattering.

Conflict of interest The authors declare no competing financial interests.

Bo Peng received his BSc (Honors) from Lanzhou University in 2005, and obtained his PhD degree from the Technical Institute of Physics and Chemistry, Chinese Academy of Sciences in 2010. He did his postdoctoral research in Singapore between 2010 and 2015. He is currently the Head of the Magneto-optical 2D Materials Group in the University of Electronic Science and Technology of China. His research is focused on the 2D ferromagnetic materials toward spintronics and valleytronics.

Kai Guo received his BSc from the University of Electronic Science and Technology of China in 2017. He focuses his research on the Raman studies of 2D ferromagnetic CrI_3.

本征铁磁二维材料CrI_3层间堆叠结构层数依赖性研究

郭锴[1,4], 邓博文[3], 刘镇[1,4], 高超峰[2], 石钟太[1,4], 毕磊[1,4], 张丽[1,4], 陆海鹏[1,4], 周佩珩[1,4], 张林博[1,4*], 程迎春[2], 彭波[1,4*]

摘要 二维体系中的长程铁磁序现象再次打破了Mermin-Wagner理论. 铁磁二维材料的铁磁性与层层堆叠的顺序、结构、层间距息息相关. 目前对铁磁二维材料CrI_3在低温下的堆叠顺序和结构仍不确定, 且未见报道. 针对该科学问题, 本工作深入研究了2–5层及块体CrI_3的拉曼特征, 详细研究了拉曼特征峰与层数、偏振、旋光和温度之间的依赖关系; 揭示了2–5层及块体CrI_3在低温下(10 K)为菱方堆叠结构, 解决了领域内关于CrI_3低温结构的争议, 填补了该领域的研究空白, 并发现了自旋声子耦合现象. 本工作开创了独特的磁光电原位传输测量系统, 从样品制备到表征完全与空气隔绝, 避免样品污染和损坏, 因此, 本工作更准确地表征出了CrI_3最本征的结构特性.

